Tunneling motion and splitting in the CH2OH radical: (Sub-)millimeter wave spectrum analysis

L. Coudert, O. Chitarra, J.-T. Spaniol, J.-C. Loison, M.-A. Martin-Drumel, O. Pirali

Tunneling motion and splitting in the CH_2OH radical: (sub-)millimeter wave spectrum analysis

L. H. Coudert,[1, a)] O. Chitarra,[1] J.-T. Spaniol,[1] J.-C. Loison,[2] M.-A. Martin-Drumel,[1] and O. Pirali[1]
[1)] *Université Paris-Saclay, CNRS, Institut des Sciences Moléculaires d'Orsay, 91405 Orsay, France*
[2)] *Institut des Sciences Moléculaires, UMR 5255 CNRS - Université de Bordeaux, Bât. A12, 351 Cours de la Libération, 33405 Talence cedex, France*

(Dated: 17 May 2022)

The (sub-)millimeter wave spectrum of the non-rigid CH_2OH radical is investigated both experimentally and theoretically. *Ab initio* calculations are carried out to quantitatively characterize its potential energy surface as a function of the two large amplitude $\angle H_1COH$ and $\angle H_2COH$ dihedral angles. It is shown that the radical displays a large amplitude torsional-like motion of its CH_2 group with respect to the OH group. The rotation-torsion levels computed with the help of a 4-D Hamiltonian accounting for this torsional-like motion and for the overall rotation exhibit a tunneling splitting, in agreement with recent experimental investigations, and a strong rotational dependence of this tunneling splitting on the rotational quantum number K_a due to the rotation-torsion Coriolis coupling. Based on an internal axis method approach, a fitting Hamiltonian accounting for tuneling effects and for the fine and hyperfine structure is built and applied to the fitting of the new (sub)-millimeter wave transitions measured in this work along with previously available high-resolution data. 778 frequencies and wavenumbers are reproduced with an unitless standard deviation of 0.79 using 27 parameters. The $N = 0$ tunneling splitting, which could not be determined unambiguously in the previous high-resolution investigations, is determined based on its rotational dependence.

I. INTRODUCTION

Although molecules displaying either a large amplitude motion or an unpaired electron have been the subject of numerous spectroscopic investigations, far fewer molecules displaying both features have been spectroscopically characterized. These include sodium trimer (Na_3), exhibiting both a pseudorotation tunneling motion and an electron spin-pseudorotation coupling,[1] the acetyl radical (CH_3CO), in which the methyl group internal rotation is coupled to the fine structure,[2] and the triatomic methylene (CH_2) and amidogen (NH_2) radicals in which an electron spin-rotation coupling takes place in addition to a large amplitude bending motion.[3,4]

The present paper deals with the hydroxymethyl radical (CH_2OH) presenting both an unpaired electron and a large amplitude motion. This astrophysically relevant species has not been detected yet in the interstellar medium although its isomeric form CH_3O has.[5] The spectrum of the hydroxymethyl radical was first observed at low resolution using infrared (IR) matrix isolation spectroscopy.[6,7] The assignment to the radical was confirmed by the satisfactory agreement between observed and calculated vibrational frequencies provided by an approximate valence force field. Although the hydroxymethyl radical is a short-lived, reactive species, difficult to observe in the lab, it has since been the subject of several infrared and microwave spectroscopic investigations. Its infrared spectrum was recorded, with a higher resolution than in the pioneering investigations,[6,7] by Feng *et al.*[8] who observed several vibrational bands with a partially resolved rotational structure thanks to double resonant ionization detected IR spectroscopy. Nearly ten years later, a fully rotationally resolved absorption spectrum was reported by Roberts *et al.*[9] for the symmetric CH stretch ν_3 fundamental band. The values of the rotational constants B and C could be determined for the ground and excited vibrational states along with an accurate band center. The first pure rotational spectrum of the radical was measured by Bermudez *et al.*[10] who assigned nearly one hundred transitions with $K_a = 0$ and 1 in the millimeter wave domain and observed a tunneling splitting for the first time. In the subsequent investigation of Schuder *et al.*,[11] tunneling and electron spin-rotation splittings were observed for several rotational components of the ν_3 band. Since then, more than 150 new pure rotational transitions have been measured in the millimeter wave domain by Chitarra *et al.*[12] also for $K_a = 0$ and 1. The high-resolution data[10–12] were interpreted in terms of a slightly asymmetric top molecule with rotational levels split into several components due to the fine and hyperfine couplings and to the tunneling. The rotational dependence of the tunneling splitting was ignored and a constant tunneling splitting of about 150 MHz was assumed. For the fine and hyperfine couplings, the splittings were found to be on the order of 100 MHz.

Early *ab initio* calculations[13–15] revealed that the hydroxymethyl radical is a non-rigid species exhibiting a complicated potential energy surface (PES) where 3 stationary points, shown in Fig. 1, were found: a C_1 minimum (S), a planar local maximum (m) 300 cm^{-1} higher, and a pyramidal C_s saddle point (M) 1500 cm^{-1} above the minimum. The subsequent *ab initio* calculations of

[a)] Electronic mail: laurent.coudert@universite-paris-saclay.fr

Schuder *et al.*[11] were consistent with a large amplitude motion of the radical that can be pictured as an internal rotation of the CH_2 group, exchanging its two hydrogen atoms and hindered by a two-fold symmetry potential.

In this paper, the rotation-tunneling energy levels of the CH_2OH radical are investigated and its high-resolution spectrum is analyzed. New transitions measured in the (sub-)millimeter wave domain are reported which, compared to the previous millimeter-wave measurement,[10,12] extend the frequency and K_a-value ranges and include the astrophysically relevant $1_{10} \leftarrow 1_{01}$ cold transition. Starting from an *ab initio* PES, the radical energy level diagram is first quantitatively described using a 4-D model in which the large amplitude torsional motion and the overall rotation of the molecule are treated simultaneously; the torsional motion and the hindering potential being determined from the *ab initio* PES. This preliminary calculation allowed us to assign the appropriate symmetry label to the rotation-tunneling levels and revealed that a strong rotational dependence of the tunneling splitting takes place.[16] Using then an internal axis method (IAM) formalism,[17,18] a fitting approach is build which accounts for the effects of the large amplitude motion and for the fine and hyperfine couplings. With this approach, a line position analysis of the already available[10–12] microwave and infrared data and of the newly measured sub-millimeter wave transitions is carried out. A total of 778 transitions are reproduced with a unitless deviation of 0.79 using 27 parameters. These include the magnitude of the tunneling splitting which could be determined unambiguously exploiting its rotational dependence.

The paper has four remaining sections. In Section II, the experimental setup used for the new measurements is described. In Section III, a qualitative description of the two-dimensional PES of the radical is given and rotation-tunneling energies are deduced. The fitting approach is described in Section IV and the analysis results are given in Section V. Section VI is the discussion.

II. EXPERIMENTAL SPECTRUM

In this work, the CH_2OH radical was synthesized from methanol using an H abstraction technique where F atoms, produced by a microwave discharge, are injected into a reaction cell where they collide with the precursor.[19] To record new pure rotational transitions of the radical, we used an upgraded version of the absorption experimental set-up described in Chitarra *et al.*[12] The upgrade consists in three points: i) multiple injections of F atoms along the cell for increased radical production; ii) longer absorption path length by implementing double-pass; and iii) a fast identification of transitions belonging to open-shell species thanks to Zeeman modulation. The main aspects of the set-up and data acquisition are described in the following and a detailed description will be presented in a subsequent paper.

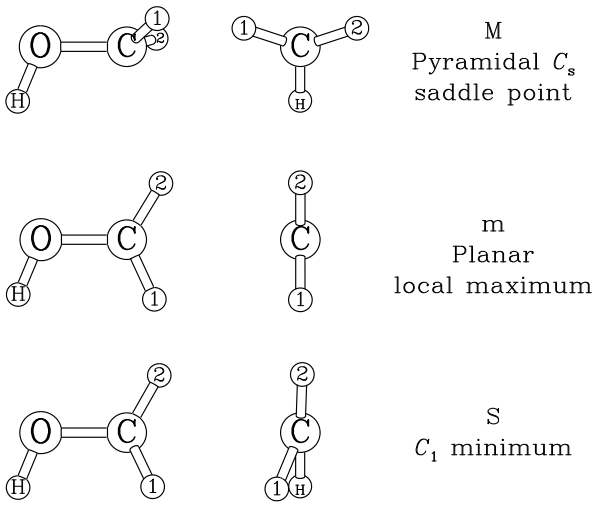

Figure 1. Geometry of the stationary points displayed by the hydroxymethyl radical potential energy surface. The two methylenic hydrogen atoms, H_1 and H_2, are labeled 1 and 2, respectively. For the geometries in the left column, the COH atoms are contained in the figure plane. For the geometries in the middle column, the CO bond is perpendicular to this plane. The letters M, m, and S are shorthand notations for the stationary points.

F atoms are produced by a 100 W microwave discharge in an F_2/He mixture (5 % dilution) and injected into the reaction cell through three separate inlets distant by 30 cm. The reaction cell is a 2 m long Pyrex cell covered by a fluorinated wax to limit surface reactions and equipped with a Teflon window on one end. The optimization of CH_2OH signal led to partial pressures of about 5 μbar of methanol and 25 μbar of F_2/He.

The (sub-)millimeter radiation is generated by a radio-frequency synthesizer (Rhodes & Schwarz), referenced to a Rubidium atomic clock, feeding a solid-state frequency multiplication chain (Virginia Diode Inc., VDI). It allows for a broad tunability, covering here the 140–900 GHz spectral range. A wire grid polarizer (5 μm diameter and 22 μm spacing wires, PureWavePolarizers Ltd.) and a roof-top mirror allow for a double pass of the collimated radiation into the absorption cell; an off-axis parabolic mirror focuses the output radiation onto the detector. Between 140 and 330 GHz, we used Schottky diode detectors (VDI) and, at higher frequencies, a liquid Helium cooled InSb hot electron bolometer detector (Infrared Labs) operating at 4 K. For all recordings, the frequency modulation of the (sub-)millimeter radiation was set to 48.157 kHz. Because of increasing values of the Doppler linewidths with increasing frequencies, both the modulation depth and frequency steps were adjusted based on the spectral range; they were set to values ranging from 500 to 1800 kHz and from 50 to 200 kHz, respectively. Relatively long acquisitions were required to achieve reasonable signal-to-noise ratio on CH_2OH lines, typically from 4 to 16 s per frequency point.

To perform Zeeman modulation, an alternating current

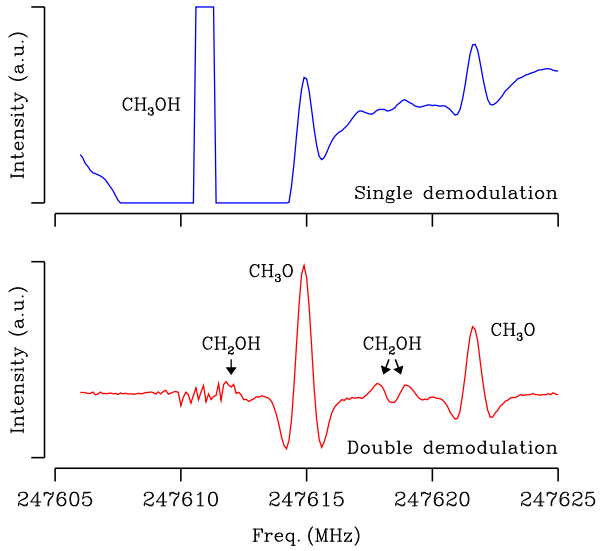

Figure 2. Example of a recording in the 247605–247625 MHz range. The top (bottom) trace displays the spectrum at the first (second) demodulation stage. On the top trace, the signal is dominated by a strong line of methanol (about 1000 times stronger than the neighboring features but saturated at the sensitivity level of the lock-in) and the resulting baseline variation. On the bottom trace, transitions of open-shell species are clearly visible over a flat baseline. Two lines of CH_3O and three lines of CH_2OH are seen. Residual noise in the region of the strong CH_3OH absorption (most likely induced by saturation effects) clearly affects the lowest frequency transition of CH_2OH.

(at a 71 Hz frequency) circulates through an 800-spires coil, wrapped along approximately 1.3 m of the reaction cell length, resulting in an alternating magnetic field of $\sim$ 20 Gauss. The alternating current is generated by a waveform generator followed by an audio amplifier (Analogue Associated) and a diode. As evidenced by Fig. 2, the double modulation scheme essentially acts as a filter for both close-shell species contribution and baseline effect.

Two lock-in amplifiers (Ametek and Stanford Research), connected in series, perform the signal recovery. The first lock-in demodulates the signal at the second harmonic of the source frequency modulation while the second one demodulates the source-frequency-demodulated signal at the magnetic field modulation frequency. Both signals are retrieved by the acquisition computer.

Using this set-up, 464 pure rotational transitions of CH_2OH have been measured with a line position accuracy ranging from 30 to 800 kHz. It should be stressed that the magnetic field modulation is key to the assignments carried out in this work. It allows us to discriminate the weak CH_2OH lines from the numerous strong transitions of the precursor and of the reaction products, mainly H_2CO.

III. ENERGY LEVELS CALCULATION

Ab initio calculations are carried out and show that the large amplitude torsional motions can be parameterized in terms of a single large amplitude angular-type coordinate. The corresponding hindering potential is also retrieved from these *ab initio* calculations. These results are used to compute rotation-torsion energy levels with the help of a 4-D model accounting for the large amplitude motion and the overall rotation. The spin of the unpaired electron is ignored in this preliminary energy levels calculation.

In non-rigid molecules displaying internal rotation of a methyl group, the torsional motion can be pictured as a rigid methyl group undergoing internal rotation with respect to a rigid frame; the axis of internal rotation remaining parallel to the three fold symmetry axis of the methyl group and fixed with respect to this frame. Such a description is appropriate for methanol,[20] which is a benchmark molecule for hindered rotation, but not for the CH_2OH radical because its OCH_2 group does not remain rigid during the large amplitude motion. As emphasized by the previous[11,13–15] and present *ab initio* calculations, the geometry of this group changes and the line bisecting the HCH bond angle, which might be taken as the axis of internal rotation, does not remain parallel to the CO bond.

A. Potential energy surface

Using the Gaussian 16 package,[21] a two-dimensional *ab initio* PES was calculated in the two angles $\xi_1 = \angle H_1COH$ and $\xi_2 = \angle H_2COH$, where the two dihedral angles are defined with the atom labeling of Fig. 1. The ωB97X-D/cc-pVTZ level of theory was chosen and the remaining 7 internal coordinates were optimized. The two-dimensional surface was calculated for ξ_1 and ξ_2 such that $\xi_1 - \xi_2 - \pi \mod 2\pi$ is in the range -40 to $+40°$ allowing us to explore energy values below 5000 cm^{-1}. A contour plot of the surface is shown in Fig. 3 where the contours span energy values ranging from 0 to 1900 cm^{-1} only. The stationary points, described in the previous *ab initio* calculations[11,13–15] and shown in Fig. 1, are indicated in Fig. 3. The lines of steepest descent, also shown in this figure, connect these stationary points.

Along the line of steepest descent, ξ_1 and ξ_2 are expressed in terms of two functions $\xi_1^s(\eta)$ and $\xi_2^s(\eta)$, depending on the variable η, such that the derivative vector with components $\xi_1^{s\prime}(\eta)$ and $\xi_2^{s\prime}(\eta)$ is parallel to the gradient of the potential energy function. Figure 3 emphasizes that following the line of steepest descent allows us to reach the non-equilibrium configurations of the radical that are important for the tunneling energy level calculation. This suggests that the harmonic approximation[22–24] should be made and that the 9 internal coordinates of the radical should be replaced by the single angular-type large amplitude coordinate η and 8

Table I. Structural parameters[a] and stationary points energy

η	ξ_1	ξ_2	SP[b]	E[c]
MP3/6-31G** level of theory[13]				
0.0	0.0	−180.0	m	32
15.7	33.3	−181.9	S	0
90.0	104.8	−104.8	M	1392
CCSD(T)/pVTZ level of theory[14,15]				
0.0	0.0	−180.0	m	140
9.3	23.9	−185.3	S	0
90.0	-	-	M	1643
CCSD(T)/aVQZ level of theory[11]				
0.0	0.0	−180.0	m	96
90.0	-	-	M	1661
ωB97X-D/cc-pVTZ level of theory (*this work*)				
0.0	0.0	−180.0	m	96
8.6	22.2	−185.0	S	0
90.0	100.2	−100.2	M	1711

[a] The angles η, ξ_1, ξ_2 are given in degrees.
[b] The letter identifying the stationary points is listed in this column.
[c] *Ab initio* energies are given in this column in cm^{-1}.

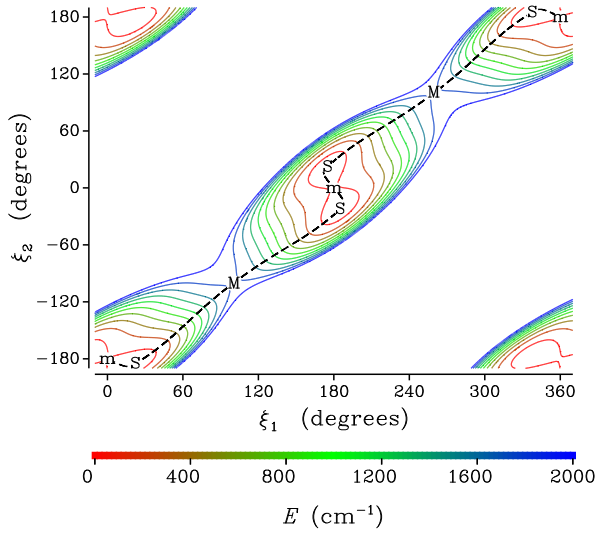

Figure 3. A contour plot of the potential energy surface of CH_2OH. The coordinates used are the angles ξ_1 and ξ_2 which are shorthand notations for the dihedral angles $\angle H_1COH$ and $\angle H_2COH$. 10 contours with color-coded energies E are drawn with solid lines. Energy value are equally spaced from 100 to 1900 cm^{-1}. Stationary points are indicated by the letters M, m, and S; the latter being the minimum. The lines of steepest descent are drawn with a dashed line.

small amplitude coordinates. The coordinate η is taken such that $0 \leq \eta \leq 2\pi$. Symmetry considerations allow us to express $\xi_1^s(\eta)$ and $\xi_2^s(\eta)$ in the following way:

$$\begin{cases} \xi_1^s(\eta) = \eta + f(\eta), \\ \xi_2^s(\eta) = \eta - \pi - f(\eta), \end{cases} \tag{1}$$

where $f(\eta)$ is an odd function of η with 2π periodicity fulfilling $f(\pi-\eta) = f(\eta)$. Equations (1) allow us to write η and $f(\eta)$ as:

$$\begin{cases} \eta = [\xi_1^s(\eta) + \xi_2^s(\eta) + \pi]/2, \\ f(\eta) = [\xi_1^s(\eta) - \xi_2^s(\eta) - \pi]/2. \end{cases} \tag{2}$$

In the case of a C_{2v} rigid OCH_2 group rotating about its CO bond, the relation $\xi_1 - \xi_2 - \pi = 0$ would hold, the function $f(\eta)$ would be zero, and η would be the angle of internal rotation of the CH_2 group with respect to the hydroxyl group. The second of Eqs. (2) implies that $f(\eta)$ is a measure of how much the OCH_2 group departs from C_{2v} symmetry. There is no analytical expression for $f(\eta)$ which was retrieved from the *ab initio* calculations and its variations are depicted in Fig. S1, available in the supplementary material. As emphasized by this figure, $f(\eta)$ displays strong variations near stationary point m corresponding to $\eta = 0$, π, and 2π. Table I compares η, ξ_1, ξ_2 values and energies for the stationary points found in the previous[11,13–15] and present *ab initio* calculations. For stationary point S, the smallest value of η was found in this work. For stationary point m, the energy value retrieved in this work is in between those reported in the early investigations[13–15] and equal to that found more recently.[11] For stationary point M, the energy obtained in this work is higher than those previously reported and the closest to that of Schuder *et al.*[11]

B. Torsional motion and hindering potential

Using the atom labeling of Fig. 1, the three bond angles and four bond lengths are expressed in terms of η. For the bond angles $\angle H_1CO$ and $\angle H_2CO$, we find:

$$\begin{cases} \angle H_1CO = \sum_{i=0}^{n_b} b_i \cos i\eta, \\ \angle H_2CO = \sum_{i=0}^{n_b} b_i (-1)^i \cos i\eta, \end{cases} \tag{3}$$

where b_i, with $0 \leq i \leq n_b$, are expansion coefficients. For the bond angle $\angle COH$, we obtain:

$$\angle COH = \sum_{i=0}^{n_c} c_{2i} \cos 2i\eta, \tag{4}$$

where c_{2i}, with $0 \leq i \leq n_c$, are expansion coefficients. For the $r(CH_1)$ and $r(CH_2)$ bond lengths, equations similar to Eqs. (3) arise. Finally, for both the $r(CO)$ and $r(OH)$ bond lengths, an equation similar to Eq. (4) can be used. The parameterization in Eqs. (1), (3), and (4) ensures that hydrogen atoms H_1 and H_2 are equivalent. The transformation $\eta \to \eta \pm \pi$ interchanges the two hydrogen

atoms as it leads to $\xi_1 \leftrightarrow \xi_2$, $\angle H_1CO \leftrightarrow \angle H_2CO$, and $r(CH_1) \leftrightarrow r(CH_2)$. The parameterization in Eqs. (1), (3), and (4) also ensures that molecular configurations characterized by η and $2\pi - \eta$ are mirror images from each other. The expansion parameters in Eqs. (3) and (4) were fitted to the present *ab initio* results and are their values reported in Table S1 available in the supplementary material.

The hindering potential $V(\eta)$ was computed as the electronic energy retrieved in Section III A plus the zero-point energy arising from the small amplitude modes. In addition to the contribution from the 7 modes corresponding to the three bond angles and four bond lengths, the contribution from ν_8, a mode corresponding to small variations $\delta\xi_1$ and $\delta\xi_2$ of the two dihedral angles, was also taken into account. Describing ν_8 with the small amplitude coordinate δq_8, the small variations of the two dihedral angles are then:

$$\begin{cases} \delta\xi_1 = -[1 - f'(\eta)]\delta q_8, \\ \delta\xi_2 = +[1 + f'(\eta)]\delta q_8. \end{cases} \quad (5)$$

This equation ensures that the ν_8 mode is not redundant with that corresponding to small variations of η. Figure 4 depicts the variations of the hindering potential $V(\eta)$. It displays two barriers at $\eta = \pi/2$ and $3\pi/2$ characterized by a height of 1600 cm^{-1} and corresponding to stationary point M. At $\eta = 0$, π, and 2π, there arise three local maxima corresponding to stationary point m with a barrier height of 60 cm^{-1}. Near these local maxima, strong variations of the hindering potential are observed. The hindering potential $V(\eta)$ retrieved in this work is quantitatively close to that of Schuder *et al.*[11] plotted in their Fig. 9. When comparing the two figures, it should be kept in mind that the relation $\phi_{COH} = \eta + \pi/2$ holds between the large amplitude coordinate used by these authors and that used in this work.

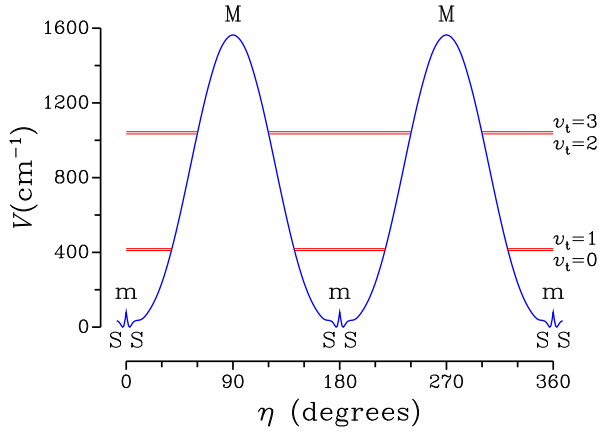

Figure 4. The hindering potential $V(\eta)$ in cm^{-1} is plotted as a function of the large amplitude coordinate η in degrees. The letters M, m, and S identify the stationary points described in Fig. 1 and in Section III A. Horizontal lines indicate the $N = 0$ torsional levels, reported in Section III C, labeled with the torsional quantum number v_t. The tunneling splitting between the $v_t = 0, 1$ and $2, 3$ pairs of levels has been greatly increased for clarity.

C. Rotation-torsion energy levels

Rotation-torsion energy levels were computed using the usual Eulerian angles χ, θ, ϕ to describe the orientation of the xyz molecule-fixed axis system with respect to the laboratory-fixed axis system. The molecule-fixed axis system is attached to the molecule so that the carbon atom is located at the origin. The COH group is contained in the xz-plane with the CO bond coinciding with the z-axis and pointing in the same direction as this axis. The hydrogen atom of this group is characterized by a negative x-value. Altering the atom coordinates with the η-dependent transformation given in Eq. (2) of Lauvergnat *et al.*[25] ensures that the center of mass of the molecule is at the origin of the molecule-fixed axis system. The permutation-inversion symmetry group to be used for the non-rigid hydroxymethyl radical is G_4 consisting of $\{E, (12)^*, (12), E^*\}$ and isomorphic to C_{2v}. The effects of the various permutation-inversion symmetry operation on the large amplitude coordinate η and on the Eulerian angles χ, θ, ϕ are given in Table II along with the G_4 character table.

A 4-D rotation-torsion Hamiltonian $H_{r\text{-}t}$ is derived using the same ideas as in Section 4.1 of Lauvergnat *et al.*[25] Starting from $\mathbf{I}(\eta)$ the generalized 4×4 inertia tensor,[26] the 4×4 inverse inertia tensor $\boldsymbol{\mu}(\eta)$ is obtained and allows us to obtain the kinetic energy part of $H_{r\text{-}t}$. The rotation-torsion Hamiltonian is then:

$$H_{r\text{-}t} = \tfrac{1}{2} \sum_{\alpha,\beta} N_\alpha \, \mu(\eta)_{\alpha\beta} \, N_\beta + V(\eta), \quad (6)$$

where $\alpha, \beta = x, y, z$, and η; N_x, N_y, and N_z are molecule-fixed components of the rotational angular momentum; $N_\eta = -i\partial/\partial\eta$ is the momentum conjugate to η; $\mu(\eta)_{\alpha\beta}$ are the components of the generalized inverse inertia tensor $\boldsymbol{\mu}(\eta)$; and $V(\eta)$ is the hindering potential retrieved in Section III B. As emphasized by Eq. (6), the pseudopotential term given in Eq. [10] of Mekhtiev *et al.*[26] is ignored. The volume element to be used for $H_{r\text{-}t}$ is $d\eta \sin\theta d\theta d\phi d\chi$.

The results given in Sections 4.2 and 4.3 of Lauvergnat *et al.*[25] for the internal rotation of the CH_2DOH molecule can also be used in the present investigation. The higher symmetry of the CH_2OH internal rotation problem compared to that of CH_2DOH leads to a few changes concerning the form of the torsional functions and the expression of the torsional matrix elements. The torsional functions introduced in Eq. (15) of Lauvergnat *et al.*[25] should be replaced by two symmetry adapted torsional functions, distinguished by the superscripted letters A and B, which

Table II. Coordinate transformations and G_4 character table

PI[a]	E	(12)	E^*	$(12)^*$
Tunneling[b]	η	$\eta+\pi$	$2\pi-\eta$	$\pi-\eta$
Rotation[c]	R^0	R^0	R_y^π	R_y^π
A_1	+1	+1	+1	+1
A_2	+1	+1	−1	−1
B_1	+1	−1	−1	+1
B_2	+1	−1	+1	−1

[a] Permutation-inversion operations.
[b] Effects of the permutation-inversion operations on the large amplitude coordinate η.
[c] Effects of the permutation-inversion operations on the Eulerian angles. R^0 and R_y^π are shorthand notations for the identity and the transformation $\chi,\theta,\phi \rightarrow \pi-\chi,\pi-\theta,\pi-\phi$, respectively.

are the following:

$$\begin{cases} \phi^A_{Nk,v_t}(\eta) = \sum\limits_{n=-n_t}^{n_t} A_n^{Nk,v_t}|2n\rangle, \\ \phi^B_{Nk,v_t}(\eta) = \sum\limits_{n=-n_t}^{n_t} B_n^{Nk,v_t}|2n+1\rangle, \end{cases} \quad (7)$$

where A_n^{Nk,v_t} and B_n^{Nk,v_t} are expansion coefficients; $|n\rangle = \exp(in\eta)/\sqrt{2\pi}$ are free internal rotation functions; and n_t is a positive integer corresponding to the size of the torsional matrix. The G_4 symmetry operation (12) has no effect on the torsional function $\phi^A_{Nk,v_t}(\eta)$, but changes $\phi^B_{Nk,v_t}(\eta)$ into its negative value because of the $e^{i\pi}$ factor arising from the free internal rotation function. When using the results of Lauvergnat *et al.*,[25] the next step is setting up the matrix of the rotation-torsion Hamiltonian. This requires evaluating torsional matrix elements of the potential energy function and of the generalized inverse inertia tensor components. For the potential energy function and for components which are an even function of η, Eq. (19) of Lauvergnat *et al.*[25] can be used. For components which are an odd function of η, Eq. (24) of the same authors can be used. In these equations, the function $F(\alpha)$ should be replaced by $F(\eta)$ displaying π-periodicity because of the higher symmetry of the CH_2OH internal rotation problem compared to that of CH_2DOH. As a result, the coefficients g_p in Eqs. (19) and (25) of Lauvergnat *et al.*[25] vanish when p is odd.

Spinless rotation-torsion energies were calculated using the parameterization of the internal coordinates and the expansion potential retrieved in Section III B. Since the potential energy function displays two energetically equivalent minima, the calculation should lead to pairs of close lying levels split by the tunneling splitting. Calculated energies are listed up to $N = 3$ in Table III where rotation-torsion levels are labeled using the usual rotational quantum numbers NK_aK_c, the torsional quantum number $v_t \geq 0$, and their rotation-torsion G_4 symmetry species. For $N = 0$ the maximum value of v_t is 3 and there arise two pairs of levels separated by a vibrational energy of 6.029 THz (201 cm^{-1}). For the lower and upper pairs, consisting of the $v_t = 0$ and 1; and of the $v_t = 2$ and 3 levels, respectively, the tunneling splittings are 88 and 974 MHz. The splitting found for the lower pair is about half that calculated by Schuder *et al.*,[11] listed in their Table VII. For the vibrational energy, the value obtained in this work is closer to that of Marenich and Boggs,[14,15] 281 cm^{-1}, than to that of Schuder *et al.*,[11] 329 cm^{-1}. For $N > 0$, Table III only reports the $v_t = 0$ and 1 lower pair of levels. A strong rotational dependence of the tunneling splitting with the rotational quantum number K_a can be seen. For $K_a = 0$, the tunneling splitting remains close to 88 MHz, with the $v_t = 0$ sublevel below $v_t = 1$. For $K_a = 1$, the tunneling splitting decreases down to 57 MHz, with the $v_t = 1$ sublevel now below $v_t = 0$. For $K_a = 2$, the tunneling sublevels are still inverted and the tunneling splitting is only 18 MHz. It should be pointed out that v_t values are assigned to tunneling sublevels using symmetry considerations compatible with those in Section IV A. The way v_t is defined differs from the way it is defined in the previous investigations[10–12] where $v_t = 0$ (1) is the lower (upper) tunneling sublevel. Figure 5 shows the variations with the large amplitude coordinate η of the torsional functions for $N = 0$ and $0 \leq v_t \leq 3$. The results in this figure and Table III emphasize that the CH_2OH radical is well described in the high barrier limit. The torsional functions are consistent with tunneling through the potential barriers at $\eta = \pi/2$ and $3\pi/2$. The $v_t = 0$ and 1 functions are respectively the sum and the difference of two functions localized at $\eta = 0$ and π. This also applies for the the $v_t = 2$ and 3 functions except that the localized functions display a node. The small potential barriers at $\eta = 0$, π, and 2π have little effects on the torsional functions since even the $v_t = 0$ function, which should be the most affected by these small barriers, still displays a maximum for these values of η.

IV. FITTING APPROACH

The effective IAM approach used in this investigation[17,18] allows us to express the tunneling-rotational energy in terms of several parameters to be determined by data fitting. The IAM approach accounts for the rotational dependence of the tunneling splitting, but does not allow us to predict its value from a potential energy surface. The IAM approach has already been applied to two non-rigid molecules, nitric acid (HNO_3) and difluoroboric acid (BF_2OH), displaying a large amplitude internal rotation of their OH group analogous to that in the CH_2OH radical. The theoretical results[27–29] obtained for these two molecules will be used in the following sections where the main results of the IAM approach will be recalled and the effects of the fine and hyperfine structure will be added

Table III. Spinless rotation-torsion energies[a]

N	K_a	K_c	v_t	Γ	E	N	K_a	K_c	v_t	Γ	E
0	0	0	0	A_1	0	2	2	0	1	B_2	831085
			1	B_2	88				0	A_1	831104
			2	B_1	6028934	3	0	3	0	A_2	341121
			3	A_2	6029908				1	B_1	341213
1	0	1	0	A_2	56884	3	1	3	1	B_1	497998
			1	B_1	56973				0	A_2	498056
1	1	1	1	B_1	220633	3	1	2	1	B_2	514494
			0	A_2	220689				0	A_1	514563
1	1	0	1	B_2	223382	3	2	2	1	B_2	1001338
			0	A_1	223440				0	A_1	1001356
2	0	2	0	A_1	170616	3	2	1	1	B_1	1001521
			1	B_2	170706				0	A_2	1001540
2	1	2	1	B_2	331590	3	3	1	0	A_2	1826970
			0	A_1	331647				1	B_1	1827049
2	1	1	1	B_1	339839	3	3	0	0	A_1	1826971
			0	A_2	339901				1	B_2	1827049
2	2	1	1	B_1	831049						
			0	A_2	831067						

[a] Energies calculated in Section III C are given for levels labeled with the usual rotational quantum numbers NK_aK_c, the torsional quantum number v_t, and their rotation-torsion G_4 symmetry species. Energies are given in MHz with respect to the $N = 0, v_t = 0$ level.

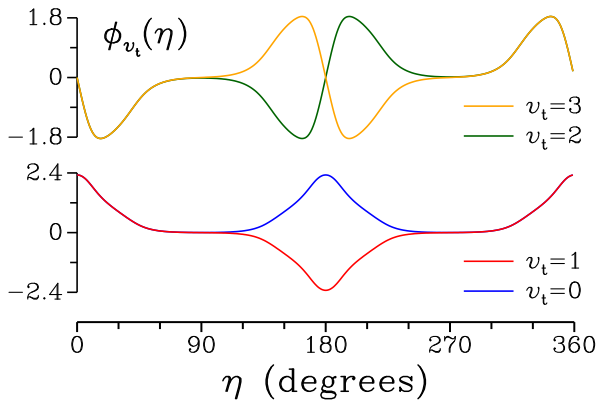

Figure 5. Variations with the large amplitude coordinate η of the torsional functions $\phi_{v_t}(\eta)$ for $N = 0$ and $0 \le v_t \le 3$. The $v_t = 2$ and 3 functions are purely imaginary and their imaginary part is plotted.

as in Coudert.[3]

A. Effective rotation-tunneling approach

The theoretical results obtained for nitric acid by Coudert and Perrin[27] can be used with only minor changes. In Eqs. (1)–(6) of this reference, the large amplitude coordinate γ should be replaced by η and the small amplitude vibrational modes should be ignored. The vibrational reference functions defined in Eq. (2) of Coudert and Perrin[27] will be written $\psi_n(\eta)$, with $n = 1$ and 2, and correspond to the two reference configurations depicted in Fig. 6 of the present paper. Although the S minimum of the two-dimensional PES has C_1 symmetry, these reference configurations are assumed planar because the $v_t = 0$ and 1 torsional levels have energies much higher than that of the local maximum m, as emphasized by Fig. 4. Also, as confirmed by Fig. 5, their torsional function is well centered around $\eta = 0$, π, and 2π. Consequently, the vibrational wavefunction $\psi_1(\eta)$ is taken even and localized about $\eta = 0$. $\psi_2(\eta) = \psi_1(\eta + \pi)$ is localized about $\eta = \pi$. The actual form of these two vibrational wavefunctions is not important, but their symmetry transformation is.[17,18] In agreement with Eq. (6) of Coudert and Perrin,[27] these vibrational wavefunctions allow us to write the reference basis wavefunctions as:

$$\Psi_{NK\alpha\, n} = \psi_n(\eta) \cdot |NK\alpha\rangle, \tag{8}$$

where $n = 1$ and 2; and $|NK\alpha\rangle$, with $0 \le K \le N$ and $\alpha = \pm 1$, are the Wang-type rotational wavefunctions defined in Eq. (1) of Coudert and Hougen.[30] They belong to the C_s symmetry species A' and A'' for $\alpha(-1)^{N+K} = +1$ and -1, respectively. The main results of the IAM approach[17,18] are the tunneling matrix elements given in Eqs. (9) and (10) of Coudert and Perrin.[27] They involve two Eulerian-type angles θ_2 and ϕ_2 describing the rotational dependence of the tunneling splitting. The tunneling matrix elements were derived adding the contribution of the two equivalent paths connecting reference Configurations 1 and 2. Between two reference basis wavefunctions of Eq. (8), the tunneling matrix elements assume the following expression:

$$\begin{aligned} H_{NK'\alpha'\,1;NK''\alpha''\,2} &= 2h_2\,(-1)^{K'} \\ &\times [\cos(K_p\phi_2)\, d^{(N)}(\theta_2)_{K',K''} \\ &+ \alpha''\cos(K_m\phi_2)\, d^{(N)}(\theta_2)_{K',-K''}], \end{aligned} \tag{9}$$

if both rotational wavefunctions belong to the same C_s symmetry species, and:

$$H_{NK'\alpha'\,1;NK''\alpha''\,2} = 0, \tag{10}$$

if the two rotational wavefunctions belong to different C_s symmetry species. In Eq. (9), h_2 is a constant corresponding to the tunneling splitting; $K_p = K' + K''$ and $K_m = K' - K''$; and $d^{(N)}(\theta)_{K,M}$ is defined in Eq. (15.8) of Wigner.[31] If either K' or K'' is equal to zero, but not both, the term on the right of Eq. (9) must be divided by $\sqrt{2}$; if both K' and K'' are equal to zero, a division by 2 is required. Tunneling-rotation energy levels are obtained using the following[27] symmetry-adapted linear combinations of the reference basis wavefunctions in Eq. (8):

$$\Psi^{v_t}_{NK\alpha} = (\Psi_{NK\alpha\,1} \pm \Psi_{NK\alpha\,2})/\sqrt{2}, \tag{11}$$

where $v_t = 0$ and 1 for the upper and lower sign, respectively. When the rotational symmetry species is A' (A''), the linear combination $\Psi^{v_t}_{NK\alpha}$ belongs to the symmetry species A_1 (A_2) and B_2 (B_1) when $v_t = 0$ and 1, respectively. The symmetry-adapted linear combinations

of Eq. (11) allow us to block diagonalize the rotation-torsion Hamiltonian into four submatrices corresponding to the G_4 symmetry species. For a given submatrix, we have the following matrix elements:

$$\begin{aligned}\langle \Psi^{v_t}_{NK'\alpha'}|H_{\text{r-t}}|\Psi^{v_t}_{NK''\alpha''}\rangle = \\ \langle NK'\alpha''|H_{\text{r}}|NK''\alpha''\rangle \pm H_{NK'\alpha'\,1;NK''\alpha''\,2},\end{aligned} \tag{12}$$

where $v_t = 0$ and 1 for the upper and lower sign, respectively; and H_{r} is the rotational Hamiltonian of either reference configurations written using the I^r representation.

The values of the angles θ_2 and ϕ_2 could be determined solving numerically Eqs. (49) of Hougen.[17] However, they were obtained here fitting the rotation-torsion energies computed in Section III C with the present rotation-tunneling approach. The analysis yielded $\theta_2 = 2.1261°$, $\phi_2 = 205.18°$, $h_2 = -24$ MHz, $A = 194$ GHz, $B = 29.8$ GHz, and $C = 27.1$ GHz. It can be seen that $4|h_2|$ is the $N = 0$ tunneling splitting. The small value of θ_2 is consistent with the slow variation of the tunneling splitting with the rotational quantum number N. Conversely, the large value of ϕ_2 is consistent with the strong variation of the tunneling splitting with the rotational quantum number K_a. The smallness of θ_2 suggests that it should be set equal to zero in Eqs. (9) and (10) in order to approximate the expression of the tunneling-rotation energy $E_{\text{r-t}}(NK_aK_c, v_t)$. This yields:

$$\begin{aligned}E_{\text{r-t}}(NK_aK_c, v_t) = \\ E_{\text{r}}(NK_aK_c) \pm 2h_2(-1)^{K_a}\cos 2K_a\phi_2,\end{aligned} \tag{13}$$

where $v_t = 0$ and 1 for the upper and lower sign, respectively; and $E_{\text{r}}(NK_aK_c)$ is the asymmetric top rotational energy. With this approximate expression, tunneling effects depend mainly on the rotational quantum number K_a. Since, as can be inferred from the symmetry species in Table III, the selection rule $\Delta v_t = 0$ holds for $\Delta K_a = 0$ parallel a-type transitions, Eq. (13) means that their line position does not depend on h_2. For $\Delta K_a = 1$ perpendicular b-type transitions, the selection rule $\Delta v_t = 0$ also holds. As can be gathered from Eq. (13), the contribution from the tunneling splitting for such transitions will be:

$$\pm 2h_2(-1)^{K'_a}[\cos 2K'_a\phi_2 + \cos 2K''_a\phi_2]. \tag{14}$$

Since ϕ_2 is different from $\pi/2$, this equation means that the tunneling parameter h_2 can be determined from the line position of perpendicular b-type transitions.

In order to account for distortion effects, the rotational Hamiltonian H_{r} in Eq. (12) is rewritten adding Watson's S-set of distortion parameters. Distortion terms are also added to the tunneling using, as in Christen *et al.*[32] and Margulès *et al.*,[33] a rotational operator D with matrix elements given by Eqs. (9) and (10) where h_2 is set to 1. With this operator, the tunneling matrix element in Eqs. (9) and (10) now reads:

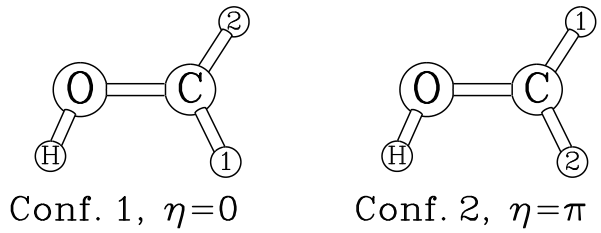

Figure 6. The two planar reference configurations to be used with the IAM approach[17,18] are drawn. Configurations 1 and 2 correspond to the vibrational reference functions $\psi_1(\eta)$ and $\psi_2(\eta)$ localized about $\eta = 0$ and π, respectively, and introduced in Section IV A.

$$\begin{aligned}H_{NK'\alpha'\,1;NK''\alpha''\,2} = \tfrac{1}{2}\langle NK'\alpha'|\{h_2 + h_{2k}N_z^2 + h_{2n}\mathbf{N}^2 \\ + f_2(N_+^2 + N_-^2) + s_{2xz}\{N_x, N_z\} + h_{2kk}N_z^4 \\ + h_{2kn}N_z^2\mathbf{N}^2 + h_{2nn}\mathbf{N}^4 + f_{2k}\{N_+^2 + N_-^2, N_z^2\}/2 \\ + f_{2n}(N_+^2 + N_-^2)\mathbf{N}^2, D\}|NK''\alpha''\rangle,\end{aligned} \tag{15}$$

where h_{2k}, h_{2n}, f_2, s_{2xz}, h_{2kk}, h_{2kn}, h_{2nn}, f_{2k}, and f_{2n} are distortion parameters; N_x, N_y, and N_z are defined as for Eq. (6); $N_\pm = N_x \pm iN_y$; and $\{,\}$ is the anticommutator.

B. Fine effects

The unpaired electron of the CH_2OH radical is accounted for adding to the rotation-torsion Hamiltonian in Eq. (12) an electron spin-rotation coupling Hamiltonian $H_{\text{s-r}}$ written using the centrifugal distortion terms corresponding to the A-reduced form of Brown and Sears.[34] We obtain:

$$\begin{aligned}H_{\text{s-r}} = \sum_{\delta=xyz}\epsilon_{\delta\delta}N_\delta S_\delta + \tfrac{1}{2}(\epsilon_{xz} + \epsilon_{zx})\{N_x, S_z\} \\ + {}^S\Delta_N\mathbf{N}^2(\mathbf{N}\cdot\mathbf{S}) + \tfrac{1}{2}{}^S\Delta_{NK}\{\mathbf{N}^2N_zS_z \\ + N_zS_z\mathbf{N}^2\} + {}^S\Delta_{KN}N_z^2(\mathbf{N}\cdot\mathbf{S}) + {}^S\Delta_K N_z^3S_z \\ + {}^S\delta_N(N_+^2 + N_-^2)(\mathbf{N}\cdot\mathbf{S}) \\ + \tfrac{1}{2}{}^S\delta_K\{(N_+^2 + N_-^2), N_zS_z\},\end{aligned} \tag{16}$$

where $\epsilon_{\delta\delta}$, with $\delta = x, y, z$, ϵ_{xz}, and ϵ_{zx} are components of the spin-rotation coupling tensor; $\mathbf{S}$, S_x, S_y, and S_z are the electron spin operator and its components; and ${}^S\Delta_N, \ldots, {}^S\delta_K$ are the distortion constants of Brown and Sears.[34] The form chosen for the electron spin-rotation operators corresponding to the non-diagonal components of the electron spin-rotation coupling tensor is appropriate for a molecule with C_s symmetry.[34]

The Wang-type rotational wavefunction $|NK\alpha\rangle$ in Eq. (8) should be replaced by the electron spin-rotation function $|NK\alpha, S, J\rangle$ characterized by the rotational quantum numbers $NK\alpha$, by S corresponding to the electron spin, and by J corresponding to the total rotational

plus spin angular momentum according to the coupling scheme $\mathbf{N}+\mathbf{S}=\mathbf{J}$. The expression given in Eq. (12) for the matrix elements of the rotation-tunneling Hamiltonian is still valid provided it is used for two rotation-spin functions characterized by the same value of the rotational quantum number N. The matrix elements of the electron spin-rotation coupling Hamiltonian $H_{\text{s-r}}$ in Eq. (16) can be found in Brown and Sears.[34] The rotation-torsion-spin levels arising after diagonalizing the rotation-torsion and rotation-spin Hamiltonians will be labeled NK_aK_c, v_t, J. The torsional quantum number v_t still is a good quantum number because it is related to the G_4 symmetry species of the wavefunction.

C. Hyperfine effects

The hyperfine coupling Hamiltonian H_{hfs} is built considering the effects of the Fermi contact and nuclear spin-electron spin dipolar interaction for all three hydrogen atoms:

$$\begin{aligned} H_{\text{hfs}} &= a_F \mathbf{I}_{\text{H}}\cdot\mathbf{S} + a_F^1 \mathbf{I}_1\cdot\mathbf{S} + a_F^2 \mathbf{I}_2\cdot\mathbf{S} \\ &\quad + \mathbf{S}\cdot\mathbf{T}\cdot\mathbf{I}_{\text{H}} + \mathbf{S}\cdot\mathbf{T}^1\cdot\mathbf{I}_1 + \mathbf{S}\cdot\mathbf{T}^2\cdot\mathbf{I}_2, \end{aligned} \tag{17}$$

where $\mathbf{I}_{\text{H}}$, $\mathbf{I}_1$, and $\mathbf{I}_2$ are respectively the hydroxyl and methylenic hydrogen atoms nuclear spin; a_F, a_F^1, and a_F^2 are the corresponding Fermi contact coupling constants; and $\mathbf{T}$, $\mathbf{T}^1$, and $\mathbf{T}^2$ the corresponding traceless nuclear spin-electron spin dipolar interaction coupling tensors. Symmetry considerations allow us to recast the hyperfine coupling Hamiltonian as the sum $H_{\text{hfs}}^s + H_{\text{hfs}}^a$, where the first (second) term involves rotation-tunneling operators that are symmetric (antisymmetric) with respect to the exchange of the two equivalent hydrogen atoms. These terms assume the following expressions:

$$H_{\text{hfs}}^s = a_F \mathbf{I}_{\text{H}}\cdot\mathbf{S} + \mathbf{S}\cdot\mathbf{T}\cdot\mathbf{I}_{\text{H}} + a_F^s \mathbf{I}_s\cdot\mathbf{S} + \mathbf{S}\cdot\mathbf{T}^s\cdot\mathbf{I}_s, \tag{18}$$

and

$$H_{\text{hfs}}^a = a_F^a \mathbf{I}_a\cdot\mathbf{S} + \mathbf{S}\cdot\mathbf{T}^a\cdot\mathbf{I}_a, \tag{19}$$

where $a_F^r = (a_F^1 \pm a_F^2)/2$; $\mathbf{T}^r = (\mathbf{T}^1 \pm \mathbf{T}^2)/2$; and $\mathbf{I}_r = \mathbf{I}_1 \pm \mathbf{I}_2$, with $r = s$ and a for the upper and lower signs, respectively. The hyperfine structure is computed using the same coupling scheme as Chitarra *et al.*,[12] $\mathbf{J}+\mathbf{I}_{\text{H}} = \mathbf{F}_1$, $\mathbf{I}_1+\mathbf{I}_2 = \mathbf{I}$, and $\mathbf{F}_1+\mathbf{I} = \mathbf{F}$. The corresponding hyperfine wavefunctions $|J, I_{\text{H}}, F_1, I, F\rangle$ are symmetric and antisymmetric with respect to the G_4 symmetry operation (12) when $I = 1$ and 0, respectively. The hyperfine structure of an NK_aK_c, v_t, J rotation-torsion-spin level can be computed considering only hyperfine wavefunctions characterized by the same value of I. In this case, for symmetry reasons, we need only evaluate the matrix elements arising from H_{hfs}^s between rotation-torsion-spin levels characterized by the same value of v_t. As shown by Eq. (18), the resulting hyperfine energies only depend on the averaged hyperfine coupling of hydrogen atoms H_1 and H_2. A more accurate computation of the hyperfine energies could be carried out considering hyperfine wavefunctions with $I = 0$ and 1. In addition to the $\Delta I = \Delta v_t = 0$ matrix elements just described, $\Delta I = \Delta v_t = 1$ matrix elements involving H_{hfs}^a would also arise. As emphasized by Eq. (19), the resulting hyperfine energy would also depend on the difference between the hyperfine coupling of hydrogen atoms H_1 and H_2. This triplet-singlet coupling depends on the value of the tunneling splitting and should be observed for rotation-spin levels with a small tunneling splitting. It should be kept in mind that the total rotation-torsion-spin-hyperfine wavefunction should belong to the B_1 or B_2 symmetry species of G_4 so as to obey the Pauli exclusion principle.

Table IV. Analysis results summary[a]

Data set	N	M	WRMS	RMS
Bermudez *et al.*[10]	94	77	0.84	0.07
Chitarra *et al.*[12]	182	147	1.04	0.08
Schuder *et al.*[11]	38	34	0.91	27.31
This work	464	249	0.54	0.18
All	778	507	0.75	6.04

[a] The data number N, the number of measured lines M, the unitless weighted root-mean-square deviation WRMS, and the root-mean-square deviation RMS in MHz are given for each data set.

V. LINE POSITION ANALYSIS

Four data sets were considered in the line position analysis, the already available millimeter wave transitions of Bermudez *et al.*[10] and Chitarra *et al.*,[12] combination differences obtained from the infrared measurements of Schuder *et al.*,[11] and the new transitions presented in Section II. This amounts to a total of 778 transitions which were least-squares fitted calculating the energy with the approach in Section IV. Transitions were given a weight equal to the inverse of their experimental uncertainty squared. For the infrared combination differences, an experimental uncertainty of 0.001 cm^{-1} was assumed. For the (sub-)millimeter wave transitions, symmetric hyperfine effects were considered in the calculation in addition to the tunneling and fine coupling effects. Unresolved multiplets consisting of several hyperfine components were treated as only one data point with a calculated frequency equal to the average value of the components frequency. For the infrared combination differences and for (sub-)millimeter wave transitions with an unresolved hyperfine pattern, hyperfine effects were ignored. The unitless standard deviation of the analysis is 0.79 varying 27 parameters. Table IV summarizes the analysis results for each data set. The observed minus calculated table is given in Table S2 available in the supplementary material. Table V lists the 50 lowest frequency

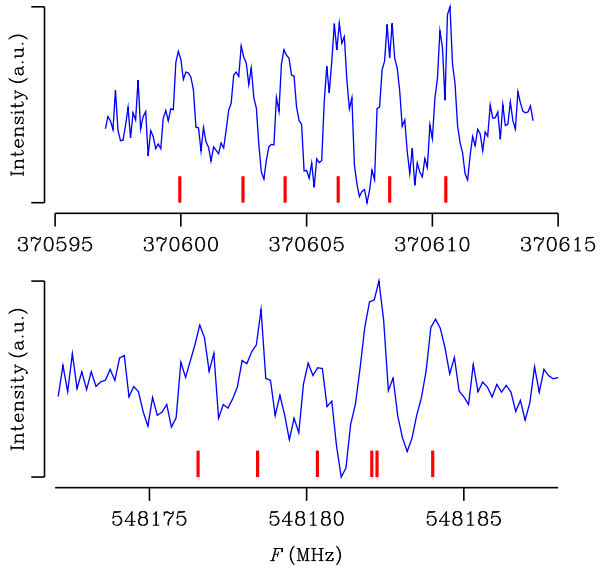

Figure 7. Doubly demodulated experimental signal for the $4_{14}, v_t = 0, J = 3.5 \leftarrow 3_{03}, 0, 2.5$ and $8_{18}, v_t = 0, J = 7.5 \leftarrow 7_{07}, 0, 6.5$ transitions at 370605 and 548181 MHz, respectively. Calculated line frequencies for the hyperfine components are indicated by vertical lines.

and the 50 highest frequency newly measured transitions sorted with increasing frequency. Both tables show that observed frequencies are reproduced within their experimental uncertainty for well resolved hyperfine patterns. This can be seen in Fig. 7 displaying portions of the observed spectrum recorded with the double demodulation technique near the $4_{14}, v_t = 0, J = 3.5 \leftarrow 3_{03}, 0, 2.5$ and $8_{18}, v_t = 0, J = 7.5 \leftarrow 7_{07}, 0, 6.5$ transitions. The fully-resolved hyperfine patterns of both transitions are well modeled. Conversely, the observed minus calculated tables show that large residuals tend to appear when the hyperfine structure is partially resolved.

Table VI gives the value of the fitted parameters. The tunneling parameter θ_2, although not fitted and constrained to the value retrieved in Section IV A, also appears in this table. Parameters not listed in Table VI were set to zero. For the fitted tunneling parameters h_2 and ϕ_2, the values in Table VI are respectively less than twice and within 0.2° from to those retrieved in Section IV A. For the tunneling parameter, the agreement is unexpectedly good since the value retrieved in Section IV A is based on low level *ab initio* calculations. A comparison between Table VI and Table 1 of Chitarra *et al.*[12] shows that the rotational constant reported for $v_t = 0$ by these authors are within 2 MHz from those determined in this work. For the electron spin-rotation constants, the agreement is even better since they differ by less than 1 MHz. For the same constants, there is also a convincing agreement with the values in Table V of Schuder *et al.*[11] In order to compare the hyperfine coupling constants determined in this work with those reported by Chitarra *et al.*,[12] it should be kept in mind that they are not labeled in the same way. The hyperfine coupling constants of the hydroxyl hydrogen atom H are labeled a_F, T_{zz}, T_{xx}, and T_{xz} in the present investigation and respectively $a_F(\mathrm{H}_1)$, $T_{aa}(\mathrm{H}_1)$, $T_{bb}(\mathrm{H}_1)$, and $T_{ab}(\mathrm{H}_1)$ in Chitarra *et al.*[12] Similarly the symmetric hyperfine coupling constants a_F^s, T_{zz}^s, T_{xx}^s, and T_{xz}^s in the present investigation correspond respectively to $a_F(\mathrm{H})$, $T_{aa}(\mathrm{H})$, $T_{bb}(\mathrm{H})$, and $T_{ab}(\mathrm{H})$ in Chitarra *et al.*[12] For the hyperfine coupling constants varied by these authors, the agreement with the value obtained in the present investigation is satisfactory. More precisely, the values reported by Chitarra *et al.*[12] for T_{xx}, a_F^s, T_{zz}^s, and T_{xx}^s are within 0.5 MHz from those in Table VI. For the hyperfine coupling constants, not varied by Chitarra *et al.*,[12] which were constrained to the *ab initio* values of Bermudez *et al.*,[10] the agreement is much less satisfactory. For a_F and T_{zz}, the hyperfine coupling constants obtained in this work are about 50% smaller than those of Chitarra *et al.*,[12] for T_{xz}, the values are opposite from each other, and T_{xz}^s was set to zero in the present analysis. This seems to indicate that the *ab initio* values of Bermudez *et al.*[10] lack accuracy.

VI. DISCUSSION

This paper aims at accounting for the spectroscopy of the CH_2OH radical which is among the few molecules displaying both a large amplitude motion and an unpaired electron studied so far under high-resolution.

Starting from a two-dimensional PES depending on the two large amplitude dihedral angles $\angle H_1COH$ and $\angle H_2COH$, it is found in Sections III A and III B that the non-equilbrium configurations of the radical can be described in terms of a large amplitude torsional-like motion. The hindering potential, retrieved in Section III B, displays π-periodicity, four minima corresponding to four C_1 configurations, and barriers with a height of 1600 cm^{-1} at the pyramidal C_s configurations. In agreement with Schuder *et al.*,[11] local maxima corresponding to small barriers with a height of 60 cm^{-1} are also found at the planar configurations. The spinless energy levels calculated in Section III C with this hindering potential display a torsional splitting of about 90 MHz for $N = 0$. This emphasizes that the high barrier limit is appropriate to describe the torsional motion of the CH_2OH radical. For $N > 0$, a strong rotational dependence of the torsional splitting is found.

The approach developed in Section IV is among the few approaches allowing us to treat a large amplitude motion in an open-shell molecule displaying electron spin-rotation coupling. It is an effective approach to be used when the large amplitude motion is an internal rotation hindered by a two-fold symmetry potential. Provided the molecule is well described in the high barrier limit, the results derived in Section IV and given in Eq. (9) emphasize that tunneling effects can be accounted for using three parameters only; one of them corresponding to the

Table V. Portion of the observed minus calculated table[a]

NK_aK_c	v_t	J	F_1	F	Obs.[b]	O−C[c]	NK_aK_c	v_t	J	F_1	F	Obs.[b]	O−C[c]
$1_{1,0}$-$1_{0,1}$	1	1.5	1		168326.534(500)	−156	$15_{0,15}$-$14_{1,14}$	0	14.5-13.5	15-14	15-14	762001.530(400)	−119
$1_{1,0}$-$1_{0,1}$	1	1.5	2		168327.577(150)	−73	$15_{0,15}$-$14_{1,14}$	0	14.5-13.5	14-13	15-14	762001.530(400)	−179
$1_{1,0}$-$1_{0,1}$	0	1.5	1	2	168602.589(200)	59	$15_{0,15}$-$14_{1,14}$	0	14.5-13.5	14-13	14-13	762001.530(400)	−542
$1_{1,0}$-$1_{0,1}$	0	1.5	2	3	168603.453(100)	43	$15_{0,15}$-$14_{1,14}$	0	14.5-13.5	15-14	14-13	762002.880(500)	−40
$1_{1,0}$-$1_{0,1}$	0	0.5	1	2	168939.050(150)	−57	$15_{0,15}$-$14_{1,14}$	0	14.5-13.5	14-13	13-12	762002.880(500)	−516
$2_{1,1}$-$2_{0,2}$	1	1.5	2		172547.803(100)	98	$15_{0,15}$-$14_{1,14}$	1	15.5-14.5	15-14		762139.174(300)	437
$2_{1,1}$-$2_{0,2}$	1	1.5	1-2		172549.555(200)	418	$15_{0,15}$-$14_{1,14}$	1	15.5-14.5	16-15		762139.174(300)	22
$2_{1,1}$-$2_{0,2}$	1	1.5	2-1		172549.555(200)	−117	$15_{0,15}$-$14_{1,14}$	1	14.5-13.5	15-14		762244.850(500)	36
$2_{1,1}$-$2_{0,2}$	1	1.5	1		172551.099(150)	−6	$15_{0,15}$-$14_{1,14}$	1	14.5-13.5	14-13		762244.850(500)	−441
$2_{1,1}$-$2_{0,2}$	0	2.5	2	1	172592.330(150)	60	$14_{1,14}$-$13_{0,13}$	1	13.5-12.5	13-12		800514.889(400)	161
$2_{1,1}$-$2_{0,2}$	0	2.5	2	2	172592.330(150)	36	$14_{1,14}$-$13_{0,13}$	1	13.5-12.5	14-13		800514.889(400)	−629
$2_{1,1}$-$2_{0,2}$	0	1.5	2	2	172818.614(200)	−44	$14_{1,14}$-$13_{0,13}$	1	14.5-13.5	14-13		800620.986(400)	−520
$2_{1,1}$-$2_{0,2}$	0	1.5	1-2	1-2	172819.337(150)	5	$14_{1,14}$-$13_{0,13}$	1	14.5-13.5	15-14		800620.986(400)	226
$2_{1,1}$-$2_{0,2}$	0	1.5	1	1	172821.610(150)	251	$14_{1,14}$-$13_{0,13}$	0	13.5-12.5	13-12	12-11	800766.152(600)	−137
$2_{1,1}$-$2_{0,2}$	0	1.5	2	1	172824.810(150)	−152	$14_{1,14}$-$13_{0,13}$	0	13.5-12.5	14-13	13-12	800766.152(600)	−927
$3_{1,2}$-$3_{0,3}$	0	2.5	2	2	178878.630(150)	−42	$14_{1,14}$-$13_{0,13}$	0	13.5-12.5	13-12	13-12	800768.685(500)	532
$3_{1,2}$-$3_{0,3}$	0	2.5	3	2	178881.062(100)	14	$14_{1,14}$-$13_{0,13}$	0	13.5-12.5	13-12	14-13	800768.685(500)	−153
$3_{1,2}$-$3_{0,3}$	0	2.5	2	1	178884.003(150)	−34	$14_{1,14}$-$13_{0,13}$	0	13.5-12.5	14-13	14-13	800768.685(500)	−198
$6_{0,6}$-$5_{1,5}$	0	5.5-4.5	6-5	7-6	192924.487(50)	25	$14_{1,14}$-$13_{0,13}$	0	13.5-12.5	14-13	15-14	800768.685(500)	−896
$6_{0,6}$-$5_{1,5}$	1	6.5-5.5	6-5		193089.192(50)	−51	$14_{1,14}$-$13_{0,13}$	0	14.5-13.5	14-13	13-12	800872.911(400)	−821
$6_{0,6}$-$5_{1,5}$	1	6.5-5.5	7-6		193090.753(50)	29	$14_{1,14}$-$13_{0,13}$	0	14.5-13.5	14-13	14-13	800872.911(400)	−309
$6_{0,6}$-$5_{1,5}$	1	5.5-4.5	6-5		193204.471(50)	16	$14_{1,14}$-$13_{0,13}$	0	14.5-13.5	14-13	15-14	800872.911(400)	−476
$6_{0,6}$-$5_{1,5}$	1	5.5-4.5	5-4		193206.544(50)	16	$14_{1,14}$-$13_{0,13}$	0	14.5-13.5	15-14	14-13	800872.911(400)	−136
$1_{1,1}$-$0_{0,0}$	0	0.5	1	2-1	220811.372(150)	−110	$14_{1,14}$-$13_{0,13}$	0	14.5-13.5	15-14	15-14	800872.911(400)	389
$11_{1,10}$-$10_{2,9}$	1	11.5-10.5	11-10		234007.318(100)	37	$14_{1,14}$-$13_{0,13}$	0	14.5-13.5	15-14	16-15	800872.911(400)	271
$11_{1,10}$-$10_{2,9}$	1	11.5-10.5	12-11		234009.122(100)	14	$16_{0,16}$-$15_{1,15}$	0	16.5-15.5	16-15	15-14	820875.270(400)	104
$11_{1,10}$-$10_{2,9}$	0	11.5-10.5	11-10	10-9	234077.717(200)	8	$16_{0,16}$-$15_{1,15}$	0	16.5-15.5	16-15	16-15	820875.270(400)	−130
$11_{1,10}$-$10_{2,9}$	0	11.5-10.5	12-11	11-10	234079.658(100)	142	$16_{0,16}$-$15_{1,15}$	0	16.5-15.5	16-15	17-16	820875.270(400)	110
$11_{1,10}$-$10_{2,9}$	0	11.5-10.5	11-10	11-10	234079.658(100)	−69	$16_{0,16}$-$15_{1,15}$	0	16.5-15.5	17-16	16-15	820875.270(400)	−181
$11_{1,10}$-$10_{2,9}$	0	11.5-10.5	11-10	12-11	234081.625(100)	−45	$16_{0,16}$-$15_{1,15}$	0	16.5-15.5	17-16	17-16	820875.270(400)	−422
$11_{1,10}$-$10_{2,9}$	0	11.5-10.5	12-11	12-11	234081.625(100)	99	$16_{0,16}$-$15_{1,15}$	0	16.5-15.5	17-16	18-17	820875.270(400)	−217
$11_{1,10}$-$10_{2,9}$	0	11.5-10.5	12-11	13-12	234083.518(150)	27	$16_{0,16}$-$15_{1,15}$	0	15.5-14.5	16-15	17-16	820966.568(400)	329
$11_{1,10}$-$10_{2,9}$	1	10.5-9.5	11-10		234256.445(100)	45	$16_{0,16}$-$15_{1,15}$	0	15.5-14.5	16-15	16-15	820966.568(400)	49
$11_{1,10}$-$10_{2,9}$	1	10.5-9.5	10-9		234258.442(150)	−32	$16_{0,16}$-$15_{1,15}$	0	15.5-14.5	15-14	16-15	820966.568(400)	−11
$11_{1,10}$-$10_{2,9}$	0	10.5-9.5	11-10	12-11	234326.294(150)	30	$16_{0,16}$-$15_{1,15}$	0	15.5-14.5	15-14	15-14	820966.568(400)	−281
$11_{1,10}$-$10_{2,9}$	0	10.5-9.5	11-10	11-10	234328.486(150)	−252	$15_{1,15}$-$14_{0,14}$	1	14.5-13.5	14-13		844456.717(750)	−250
$11_{1,10}$-$10_{2,9}$	0	10.5-9.5	10-9	11-10	234328.486(150)	171	$15_{1,15}$-$14_{0,14}$	1	14.5-13.5	15-14		844456.717(750)	−976
$11_{1,10}$-$10_{2,9}$	0	10.5-9.5	10-9	10-9	234330.926(200)	147	$15_{1,15}$-$14_{0,14}$	0	14.5-13.5			844704.611(500)	937
$11_{1,10}$-$10_{2,9}$	0	10.5-9.5	11-10	10-9	234330.926(200)	−311	$15_{1,15}$-$14_{0,14}$	0	15.5-14.5	15-14	14-13	844800.021(400)	−683
$11_{1,10}$-$10_{2,9}$	0	10.5-9.5	10-9	9-8	234333.251(150)	−49	$15_{1,15}$-$14_{0,14}$	0	15.5-14.5	15-14	15-14	844800.021(400)	−258
$8_{1,7}$-$8_{0,8}$	0	7.5	8	9	247611.887(200)	−106	$15_{1,15}$-$14_{0,14}$	0	15.5-14.5	15-14	16-15	844800.021(400)	−436
$8_{1,7}$-$8_{0,8}$	0	7.5	7	7	247617.821(100)	−91	$15_{1,15}$-$14_{0,14}$	0	15.5-14.5	16-15	15-14	844800.021(400)	−103
$8_{1,7}$-$8_{0,8}$	0	7.5	8	7	247618.996(100)	14	$15_{1,15}$-$14_{0,14}$	0	15.5-14.5	16-15	16-15	844800.021(400)	332
$7_{0,7}$-$6_{1,6}$	1	7.5-6.5	7-6		257296.070(100)	−32	$15_{1,15}$-$14_{0,14}$	0	15.5-14.5	16-15	17-16	844800.021(400)	196
$7_{0,7}$-$6_{1,6}$	1	7.5-6.5	8-7		257297.526(100)	33	$17_{0,17}$-$16_{1,16}$	0	17.5-16.5	17-16	16-15	878790.808(500)	−151
$7_{0,7}$-$6_{1,6}$	1	6.5-5.5	7-6		257433.217(100)	21	$17_{0,17}$-$16_{1,16}$	0	17.5-16.5	17-16	17-16	878790.808(500)	−327
$7_{0,7}$-$6_{1,6}$	1	6.5-5.5	6-5		257435.086(100)	30	$17_{0,17}$-$16_{1,16}$	0	17.5-16.5	17-16	18-17	878790.808(500)	−104
$2_{1,2}$-$1_{0,1}$	1	1.5-0.5	2-1		272314.772(100)	21	$17_{0,17}$-$16_{1,16}$	0	17.5-16.5	18-17	17-16	878790.808(500)	−368
$2_{1,2}$-$1_{0,1}$	0	2.5-1.5	3-2	2-1	272442.265(250)	−133	$17_{0,17}$-$16_{1,16}$	0	17.5-16.5	18-17	18-17	878790.808(500)	−550
$2_{1,2}$-$1_{0,1}$	0	2.5-1.5	2-1	2-1	272446.796(150)	−463	$17_{0,17}$-$16_{1,16}$	0	17.5-16.5	18-17	19-18	878790.808(500)	−357

[a] Assignments, observed frequencies, and observed minus calculated residuals are listed for the 50 lowest frequency and the 50 highest frequency newly measured transitions sorted with increasing frequency. Columns headed NK_aK_c, v_t, and J list respectively the rotational quantum numbers, the torsional quantum number, and the half integer rotational plus electron spin quantum number correponding to $\mathbf{J} = \mathbf{N} + \mathbf{S}$. For transitions with resolved hyperfine splittings, columns headed F_1 and F list hyperfine quantum numbers. The second one only applies for ortho levels. A dash is used to distinguish upper (left) and lower (right) level values when different.

[b] Observed frequencies in MHz and experimental uncertainties, in kHz, in parentheses.

[c] Observed minus calculated residuals in kHz corresponding to the analysis reported in Section V.

Table VI. Spectroscopic constants[a]

Parameter	Value	Parameter	Value
θ_2	2.1261[b]	ϵ_{zz}	−458.620(54)
ϕ_2	205.3522(29)	ϵ_{xx}	−121.438(13)
h_2	−42.6029(36)	ϵ_{yy}	−1.400(14)
$h_{2n}\times10^3$	−15.588(84)	${}^S\Delta_{KN}\times10^3$	13.1(12)
$f_2\times10^3$	9.03(10)	${}^S\delta_N\times10^6$	115(16)
$h_{2nn}\times10^6$	−6.89(51)	$\frac{1}{2}(\epsilon_{xz}+\epsilon_{zx})$	−48.69(20)
$f_{2n}\times10^6$	7.35(69)		
		a_F	−5.18(30)
A	194535.4966(75)	$T_{zz}\times10^3$	−596(192)
B	29843.43901(90)	T_{xx}	8.837(99)
C	25947.5409(10)	T_{xz}	−16.9(28)
D_K	5.7993(42)	a_F^s	−54.462(78)
$D_{KN}\times10^3$	587.03(16)	T_{zz}^s	−22.71(11)
$D_N\times10^3$	61.9941(51)	T_{xx}^s	19.229(63)
$d_1\times10^3$	−8.51266(93)		
$d_2\times10^3$	−1.45406(84)		

[a] Constants are given in MHz except for θ_2 and ϕ_2 which are in degrees. For fitted constants, uncertainties are given in parentheses in the same units as the last quoted digit.
[b] Constrained value

magnitude of the tunneling splitting for $N = 0$ and the remaining two describing its rotational dependence.

The main results of this investigation are presented in Section V where a line position analysis of a large body of high-resolution spectroscopic data is carried out. The data set includes previously measured millimeter wave transitions,[10,12] infrared combination differences,[11] and new sub-millimeter wave transitions measured in this work and presented in Section II. The unitless standard deviation of the analysis is 0.79 varying 27 parameters.

The value of the tunneling splitting is an important issue. In the previous millimeter wave investigations,[10,12] where only transitions with $K_a = 0$ and 1 were fitted, it was assumed that the tunneling splitting is constant and that the selection rules for the tunneling components are $\Delta v_t = 1$ in agreement with the way v_t is defined in these investigations. In order to analyze their data, Bermudez *et al.*[10] were led to use the same A rotational constant for both tunneling components and different B and C rotational constants for each tunneling components. The value retrieved by the authors for the tunneling splitting was 139 MHz. In their subsequent analysis of a larger data set, Chitarra *et al.*[12] were led to use two sets of rotational constants, one for each tunneling components. The value they retrieved for the tunneling splitting was 20 MHz larger than that of Bermudez *et al.*[10] For the limited data set considered in both analyses, the actual contribution from the A rotational constant and the tunneling is $A \mp 2h_2[\cos 2\phi_2 + 1]$ for $K_a = 1 \leftarrow 0$ b-type transitions as given by Eq. (14). This shows that the contribution from the A rotational constant and the tunneling cannot be discriminated for the limited data set considered in the previous millimeter wave investigations. In the present analysis, in agreement with the symmetry species for the reference basis wavefunctions given in Eq. (11), the selection rules for the tunneling components are $\Delta v_t = 0$. Also since the fitted transitions involve K_a values ranging from 0 to 2, we are able to discriminate the contribution from the A rotational constant and the tunneling. As evidenced by Table VI, only one set of rotational constants is used and this is because the developed fitting approach accurately models the rotational dependence of the tunneling splitting. It should be stressed that the tunneling splittings reported by Bermudez *et al.*,[10] Schuder *et al.*,[11] and Chitarra *et al.*[12] are smaller than the $N = 0$ value derived in this work, which is $4|h_2| = 170.4$ MHz.

Due to the improved experimental setup used in this work, the present re-investigation of the pure rotational spectrum of the CH_2OH radical allowed us to measure at last several transitions expected to be intense under cold interstellar conditions. Three out the four components of the $1_{10} \leftarrow 1_{01}$ transition, not detected in the previous investigations,[10,12] where thus reported in this work. As shown in Fig. 8, despite a very noisy signal due to the weakness of this transition at room temperature, unambiguous assignments and satisfactory modeling are possible. These new data, combined with the measurements published in Chitarra *et al.*,[12] should allow for a confident search of the radical in cold to warm environment of the interstellar medium.

SUPPLEMENTARY MATERIAL

See supplementary material for a figure showing the variations of the function $f(\eta)$ introduced in Section III A and for two tables. The first one reports the expansion parameters obtained with Eqs. (3) and (4); the second one gives the observed minus calculated table for the line position analysis described in Section V.

ACKNOWLEDGMENTS

Funding from the LabEx PALM (ANR-10-LABX-0039-PALM), from the Région Ile-de-France through DIM-ACAV+, and from the Agence Nationale de la Recherche (ANR-19-CE30-0017-01) is gratefully acknowledged. We acknowledge support from the Programme National "Physique et Chimie du Milieu Interstellaire" (PCMI) of CNRS/INSU with INC/INP cofunded by CEA and CNES.

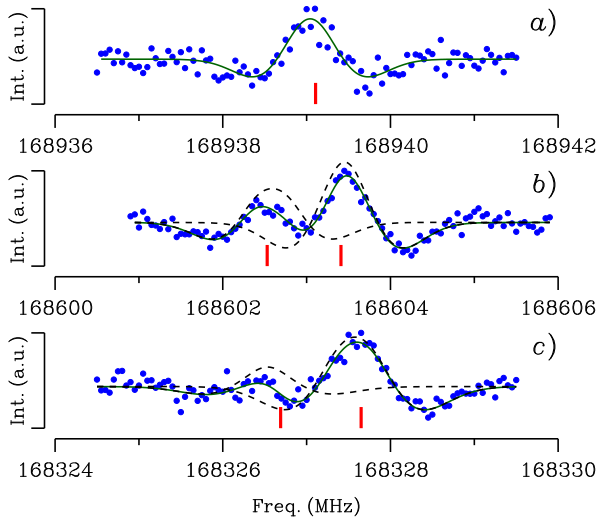

Figure 8. Experimental spectra of the fine structure and tunneling components of the astrophysically relevant $1_{10} \leftarrow 1_{01}$ transition. Panels *a*), *b*), and *c*) correspond respectively to the $v_t = 0, J = 0.5$; $v_t = 0, J = 1.5$; and $v_t = 1, J = 1.5$ components. Experimental data points are indicated by dots. Solid lines show a fit to the experimental signal using one or more Gaussian second derivative line profiles. For panels *b*) and *c*), 2 line profiles were used and each contribution is plotted using dashed lines. Calculated line frequencies are indicated by vertical lines.

DATA AVAILABILITY STATEMENT

The data that support the findings of this study are available within the article and its supplementary material.

[1] N. Ohashi, M. Tsuura, J. T. Hougen, W. E. Ernst, and S. Rakowsky, J. Mol. Spectrosc. **184**, 22 (1997).
[2] E.Hirota, A. Mizoguchi, Y. Ohshima, K. Katoh, Y. Sumiyoshi, and Y. Endo, Mol. Phys. **105**, 455 (2007).
[3] L. H. Coudert, J. Chem. Phys. **153**, 144115 (2020).
[4] M. A. Martin-Drumel, O. Pirali, and M. Vervloet, J. Phys. Chem. A **118**, 1331 (2014).
[5] J. Cernicharo, N. Marcelino, E. Roueff, M. Gerin, A. Jiménez-Escobar, and G. M. Muñoz Caro, Astrophys. J. Lett. **759**, L43 (2012).
[6] M. E. Jacox and D. E. Milligan, J. Mol. Spectrosc. **47**, 148 (1973).
[7] M. E. Jacox, Chem. Phys. **59**, 213 (1981).
[8] L. Feng, J. Wei, and H. Reisler, J. Phys. Chem. A **108**, 7903 (2004).
[9] M. A. Roberts, E. N. Sharp-Williams, and D. J. Nesbitt, J. Phys. Chem. A **117**, 7042 (2013).
[10] C. Bermudez, S. Bailleux, and J. Cernicharo, A&A **598**, A9 (2017).
[11] M. D. Schuder, F. Wang, C.-H. Chang, and D. J. Nesbitt, J. Chem. Phys. **146**, 194307 (2017).
[12] O. Chitarra, M.-A. Martin-Drumel, B. Gans, J.-C. Loison, S. Spezzano, V. Lattanzi, H. S. P. Müller, and O. Pirali, A&A **644**, A123 (2020).
[13] S. Saebø, L. Radom, and H. F. Schaefer, J. Chem. Phys. **78**, 845 (1983).
[14] A. V. Marenich and J. E. Boggs, J. Chem. Phys. **119**, 3098 (2003).
[15] A. V. Marenich and J. E. Boggs, J. Chem. Phys. **119**, 10105 (2003).
[16] C. C. Lin and J. D. Swalen, Rev. Mod. Phys. **31**, 841 (1959).
[17] J. T. Hougen, J. Mol. Spectrosc. **114**, 395 (1985).
[18] L. H. Coudert and J. T. Hougen, J. Mol. Spectrosc. **130**, 86 (1988).
[19] G. A. Garcia, X. Tang, J.-F. Gil, L. Nahon, M. Ward, S. Batut, C. Fittschen, C. A. Taatjes, D. L. Osborn, and J.-C. Loison, J. Chem. Phys. **142**, 164201 (2015).
[20] K. T. Hecht and D. M. Dennison, J. Chem. Phys. **26**, 48 (1957).
[21] M. J. Frisch, G. W. Trucks, H. B. Schlegel, G. E. Scuseria, M. A. Robb, J. R. Cheeseman, G. Scalmani, V. Barone, G. A. Petersson, H. Nakatsuji, X. Li, M. Caricato, A. V. Marenich, J. Bloino, B. G. Janesko, R. Gomperts, B. Mennucci, H. P. Hratchian, J. V. Ortiz, A. F. Izmaylov, J. L. Sonnenberg, D. Williams-Young, F. Ding, F. Lipparini, F. Egidi, J. Goings, B. Peng, A. Petrone, T. Henderson, D. Ranasinghe, V. G. Zakrzewski, J. Gao, N. Rega, G. Zheng, W. Liang, M. Hada, M. Ehara, K. Toyota, R. Fukuda, J. Hasegawa, M. Ishida, T. Nakajima, Y. Honda, O. Kitao, H. Nakai, T. Vreven, K. Throssell, J. A. Montgomery, Jr., J. E. Peralta, F. Ogliaro, M. J. Bearpark, J. J. Heyd, E. N. Brothers, K. N. Kudin, V. N. Staroverov, T. A. Keith, R. Kobayashi, J. Normand, K. Raghavachari, A. P. Rendell, J. C. Burant, S. S. Iyengar, J. Tomasi, M. Cossi, J. M. Millam, M. Klene, C. Adamo, R. Cammi, J. W. Ochterski, R. L. Martin, K. Morokuma, O. Farkas, J. B. Foresman, and D. J. Fox, "Gaussian˜16 Revision B.01," (2016), gaussian Inc. Wallingford CT.
[22] D. Lauvergnat, A. Nauts, Y. Justum, and X. Chapuisat, J. Chem. Phys. **114**, 6592 (2001).
[23] S. Blasco and D. Lauvergnat, Chem. Phys. Lett. **373**, 344 (2003).
[24] D. Lauvergnat and A. Nauts, Chem. Phys. **305**, 105 (2004).
[25] D. Lauvergnat, L. H. Coudert, S. Klee, and M. Smirnov, J. Mol. Spectrosc. **256**, 204 (2009).
[26] M. A. Mekhtiev, P. D. Godfrey, and V. Szalay, J. Mol. Spectrosc. **180**, 42 (1996).
[27] L. H. Coudert and A. Perrin, J. Mol. Spectrosc. **172**, 352 (1995).
[28] C. D. Paulse, L. H. Coudert, T. M. Goyette, R. L. Crownover, P. Helminger, and F. C. De Lucia, J. Mol. Spectrosc. **177**, 9 (1996).
[29] L. H. Coudert, P. Garcia-Fernandez, H. Mäder, J. Demaison, and J. E. Boggs, J. Phys. Chem. A **112**, 1536 (2008).
[30] L. H. Coudert and J. T. Hougen, J. Mol. Spectrosc. **139**, 259 (1990).
[31] E. P. Wigner and J. J. Griffin, *Group Theory and Its Application to the Quantum Mechanics of Atomic Spectra* (Academic Press, New York and London, 1959).
[32] D. Christen, L. H. Coudert, R. D. Suenram, and F. J. Lovas, J. Mol. Spectrosc. **172**, 57 (1995).
[33] L. Margulès, L. H. Coudert, H. Møllendal, J.-C. Guillemin, T. R. Huet, and R. Janečkovà, J. Mol. Spectrosc. **254**, 55 (2009).
[34] J. M. Brown and T. J. Sears, J. Mol. Spectrosc. **75**, 111 (1979).